

國立臺灣大學理學院天文物理研究所



碩士論文

Institute of Astrophysics

College of Science

National Taiwan University

Master Thesis

波暗物質中的潮汐剝離和孤立子震盪

Tidal stripping and soliton oscillations in fuzzy dark matter

黃立鈞

Li-Chun Huang

指導教授：薛熙于 博士

Advisor: Hsi-Yu Schive, Ph.D.

中華民國 112 年 8 月

August, 2023

國立臺灣大學碩士學位論文  
口試委員會審定書

MASTER'S THESIS ACCEPTANCE CERTIFICATE  
NATIONAL TAIWAN UNIVERSITY

波暗物質中的潮汐剝離和孤立子震盪

Tidal stripping and soliton oscillations in fuzzy dark matter

本論文係黃立鈞君(R0824404)在國立臺灣大學天文物理所完成之碩士學位論文，於民國 112 年 7 月 17 日承下列考試委員審查通過及口試及格，特此證明。

The undersigned, appointed by the Graduate Institute of Astrophysics on 17/07/2023 have examined a Master's thesis entitled above presented by Li Chun Huang (R08244004) candidate and hereby certify that it is worthy of acceptance.

口試委員 Oral examination committee:

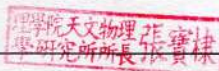
黃立鈞

(指導教授 Advisor)

林俐暉

關志鴻

系主任/所長 Director:







# Acknowledgements

謝謝在碩士生活中幫助過我的每一個人





## 中文摘要

波暗物質 (Fuzzy Datter Matter, FDM) 是一個有競爭力的暗物質候選理論，其在中心會有一個巨大的孤立子且有著大幅度密度震盪。先前的研究中指出即使周圍的暈被潮汐力給破壞掉，孤立子震盪依然存在。在本研究中我們經由自適應網格細化的三維波暗物質模擬展示了潮汐剝離是可以藉由移除孤立子的激發態去減緩震盪。減緩效率取決於軌道內主暈的平均密度和孤立子波峰密度的比率。此外當潮汐半徑相當於孤立子半徑時，孤立子就會被完全的被破壞。這些發現對於理論分析中心恆星物體因孤立子振盪所引起的加熱現象是重要的。

**關鍵字：**波暗物質、孤立子、震盪、潮汐力、潮汐剝離





# Abstract

Fuzzy dark matter (FDM) is a strong dark matter candidate, featuring a massive central soliton with large-amplitude density oscillations. Previous studies suggested that the soliton oscillations persist even after the tidal disruption of a surrounding halo. Here, via three-dimensional FDM simulations with adaptive mesh refinement (AMR), we demonstrate that tidal stripping can damp soliton oscillations by removing the soliton excited states. The damping efficiency depends on the ratio between the average enclosed density of a host halo and the soliton peak density. Furthermore, a soliton can be completely disrupted if the tidal radius is comparable to the soliton radius. These findings are important for theoretical analyses of the heating of central stellar objects owing to soliton oscillations.

**Keywords:** fuzzy dark matter, soliton, oscillation, tidal force, tidal stripping







# Contents

	<b>Page</b>
<b>Verification Letter from the Oral Examination Committee</b>	<b>i</b>
<b>Acknowledgements</b>	<b>iii</b>
<b>中文摘要</b>	<b>v</b>
<b>Abstract</b>	<b>vii</b>
<b>Contents</b>	<b>ix</b>
<b>List of Figures</b>	<b>xi</b>
<b>Chapter 1 Introduction</b>	<b>1</b>
<b>Chapter 2 Theoretical basis</b>	<b>3</b>
2.1 Soliton property . . . . .	3
2.2 Tidal potential . . . . .	4
<b>Chapter 3 Numerical method</b>	<b>7</b>
3.1 Construction of perturbed soliton . . . . .	8
3.2 Moving non-rotating frame system . . . . .	8
3.3 Simulation setup . . . . .	13
<b>Chapter 4 Simulation result</b>	<b>15</b>
4.1 Different regime . . . . .	15
4.2 Result comparison . . . . .	17

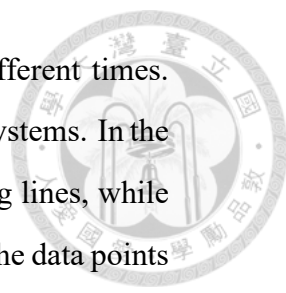
4.3	Amplitude calculation . . . . .	19
4.4	Future work . . . . .	21
<b>Chapter 5</b>	<b>Conclusion</b>	<b>23</b>
	<b>References</b>	<b>25</b>
	<b>Appendix A — tidal potential derivation and <math>\mu</math> in different frames</b>	<b>29</b>
	<b>Appendix B — calculate the amplitude</b>	<b>33</b>





# List of Figures

- 3.1 The evolution of perturbed soliton with  $\rho_c \approx 5.14e7 M_\odot kpc^{-3}$ . *Top*: Peak density of the perturbed soliton. The soliton reaches equilibrium in 0.5 Gyr. *Bottom*: Density profile of the perturbed soliton at different times. The black line represents the fitted profiles defined by Eq. (2.3) with an average  $\rho_c$ . It is evident that the cores are characterized by soliton profiles when it is stable. . . . . 9
- 3.2 The projected soliton density at different times is shown for different coordinate systems. The top panel is the inertial coordinate and the bottom panel is the moving coordinate system. During the initial stages of evolution, the deformations are quite similar between the two. However, in the later stages, as the structure becomes disrupted, tidal forces elongate the soliton into a tail-like shape. Because there are no higher-order forces in the moving coordinate system, the shapes of the tails in the two systems differ. . . . . 11

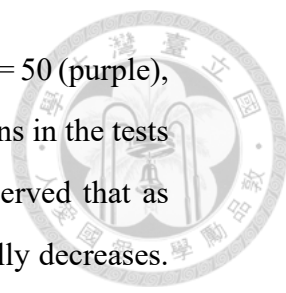


3.3 The structural evolution and relative error of soliton at different times. . . . . 12

*Top:* Density profile of soliton at different times in different systems. In the inertial coordinate system, the representation is shown using lines, while in the moving coordinate system, it is depicted using dots. The data points within the higher-density internal region are largely consistent between the two systems. Differences in data points begin to emerge in the lower-density external region. *Bottom:* Relative error in both systems at different times. The error within the interior part of the soliton is minimal, while significant error is present in the exterior. From both panels, it is evident that the data in the high-density internal region of the two systems are in agreement. This region aligns with our experimental focus. However, there are slight discrepancies in the external region, primarily due to the lower density. As a result, the relative errors are larger in this region. . . . . 12

4.1 The projected soliton density at different times is shown for three initial density ratios:  $\mu = 50, 120,$  and  $210$ . The top, middle, and bottom panels correspond to  $\mu = 210, 120,$  and  $50$ . We show time slices taken at two-gigayear intervals. When tidal forces are weak, they do not have a significant effect on the soliton core, but when they are strong, they can destroy the soliton. . . . . 16

4.2 Density profile of soliton at different times for initial density ratios  $\mu = 50, 120,$  and  $210$ . We plot the initial condition (red) and the configurations at  $t = 2.0$  (green),  $4.0$  (red),  $6.0$  (cyan), and  $8.0$  (purple) Gyr. We define the destruction of a soliton as a significant drop in central density by more than one order of magnitude. Therefore, when subjected to strong tidal forces, solitons cannot maintain their shape, and their central density drops by more than one order of magnitude, which we consider as being destroyed. However, when tidal forces are weak, solitons can maintain their shape without being destroyed. . . . . 17



- 4.3 Time evolution of peak density for the initial density ratios  $\mu = 50$  (purple), 90 (cyan), 120 (blue), 150 (green), and 210 (red). All solitons in the tests evolved from the same initial peak density. It can be observed that as time progresses, the amplitude of soliton oscillation gradually decreases. Additionally, it is evident that as the tidal force increases, the rate at which the amplitude of soliton oscillation decreases increases as well. . . . . 18
- 4.4 *Top:* Time evolution of ground state percentage for the initial density ratios  $\mu = 50$  (purple), 90 (cyan), 120 (blue), 150 (green), and 210 (red). *Bottom:* Time evolution of excited state percentage. As time progresses, the ground state percentage increases while the excited state percentage decreases. When the tidal forces increase, this process speeds up. It demonstrates that tidal forces, depending on their strength, remove the excited state over time . . . . . 21





# Chapter 1 Introduction

The concept of dark matter originated from the unexpected observation of mass in astronomical observations. As of today, dark matter has become a mainstream theory and can be used to explain phenomena such as galaxy rotation curves and gravitational lensing. Fuzzy dark matter (FDM) [9] is one of the candidates for explaining these phenomena.

FDM is described by Schrödinger-Poisson (SP) equations[20, 22, 24, 27]. It behaves like a wave and has an extremely small mass constraint, typically ranging from about  $10^{-22}$  to  $10^{-21}$  eV[1, 3, 13, 14, 28]. As a result, it exhibits a long de Broglie wavelength. FDM can explain large-scale structures as effectively as cold dark matter but offers a better explanation for small-scale structures[11, 15, 19, 20, 22, 26], such as the cusp-core problem[8, 17], the missing satellite problem[12, 16] and the too-big-to-fail problem[2, 18].

In the study of FDM, it has been observed that soliton would reside inside the halo[20] with density oscillations. Soliton exhibits a flat slope in the inner part of its density profile. If a soliton is perfect, which means it does not possess any excited states, it will not exhibit oscillation. Nonetheless, when perturbations are introduced into the system, they can trigger the formation of excited states within the soliton. These will lead to oscillatory behavior, causing the soliton to undergo periodic variations. In [5], Soliton oscillations



are closely related to their excited state.

Previous studies have investigated the impact of tidal forces on solitons. [6] examine the influences of tidal stripping and dynamical friction on FDM subhalos. [10] suggest that the decrease in the wave function's amplitude entirely characterizes the tidal mass loss process.

In this paper, we not only aim to investigate the evolution of solitons but also consider the evolution of the oscillation under the influence of tidal stripping. [21] suggested that the soliton oscillations remain persistent even in the presence of tidal disruption affecting the surrounding halo. The tidal force considered in this study is extremely small. [7] showed the mass loss rate of the soliton from tidal stripping and the survival time of satellite galaxies. The tidal force considered in this study is strong enough to destroy the soliton. These two studies provide extreme values for the strength of the tidal force. We focus on studying the effects of tidal force strength between these two papers. Specifically, we investigate how the oscillations of the soliton evolve under different tidal forces when the soliton remains intact and is not disrupted by tidal forces.

We simulate various scenarios and confirmed that tidal forces reduce the magnitude of oscillations in the soliton. Besides, we further analyze the proportion of excited state in the soliton and found that tidal forces reduce this proportion.

The structure of this paper is as follows: Chapter 2 provides the theoretical foundations required for the simulations. Chapter 3 outlines the methodology we employed. Chapter 4 presents the results and analysis of the simulations. In Chapter 5, we provide a conclusion summarizing our findings. Additionally, detailed derivations and analysis methods are included in Appendix.



## Chapter 2 Theoretical basis

In this chapter, we will discuss the properties of soliton and use the point mass assumption to derive the tidal potential as a basis for simulation. We also use the Navarro-Frenk-White (NFW) profile to derive the tidal potential. The detailed derivation is included in the appendix.

### 2.1 Soliton property

The soliton is formed by the FDM, which follows the coupled Schrödinger-Poisson (SP) equations[25, 29]

$$i\hbar\frac{\partial\psi}{\partial t} = -\frac{\hbar^2}{2m_b}\nabla^2\psi + m_a\Phi\psi, \quad (2.1)$$

$$\nabla^2\Phi = 4\pi Gm_b|\psi|^2, \quad (2.2)$$

where  $\psi$  is the wave function of FDM,  $m_b$  the particle mass of FDM,  $\Phi$  is the gravitational potential,  $m_b|\psi|^2$  is the mass density of FDM, and  $G$  is the gravitational constant. The density profile of an unperturbed soliton can be approximated by[22]

$$\rho_{soliton}(r) \approx \frac{1.9(m_b/10^{-23}eV)^{-2}(r_c/kpc)^{-4}}{[1 + 9.1 \times 10^{-2}(r/r_c)^2]^8} M_{\odot}pc^{-3}, \quad (2.3)$$

where  $r$  is the distance to the soliton center, and  $r_c$  is the radius where the density drop to half peak density. If the soliton is perturbed, it will begin to oscillate. The timescale of oscillation can be described as [4]

$$\tau_{soliton}(\rho_c) \cong 92.1 \left( \frac{\rho_c}{M_{\odot} pc^{-3}} \right)^{-1/2} Myr, \quad (2.4)$$

where  $\rho_c$  is the time-average peak density of the soliton.

## 2.2 Tidal potential

When a soliton orbits its host, It is subject to the gravitational field from the host. Due to the varying gravitational force at different positions on the soliton, tidal stripping happens. When simulated in the moving non-rotating coordinate system which we would discuss in Chapter 3, the gravitational potential is transformed into tidal potential.

Focusing on the system centered on the satellite, the tidal force pulls the soliton towards the center of mass of the host, causing it to stretch along the line connecting both. By assuming that the distance from the target point to the soliton is much smaller than the distance from the soliton to the center, and treating the host as a point mass, we can derive the acceleration and tidal potential as follow. The scale of acceleration due to tidal force is shown

$$a_r = \frac{GMr}{R^3} (2 \cos^2 \theta - \sin^2 \theta), \quad (2.5)$$

$$a_{theta} = \frac{GMr}{R^3} (3 \cos \theta \sin \theta), \quad (2.6)$$

where  $M$  is the host mass,  $R$  is the distance between the soliton and the host, and  $\theta$  is the

angle between the vector from the host to the soliton and the vector from the soliton to the target position. The tidal potential derived from Eq. 2.5 is

$$V_t = \frac{-GMr^2}{2R^3}(2\cos^2\theta - \sin^2\theta). \quad (2.7)$$

Due to the tidal potential, Eq. 2.1 becomes

$$i\hbar\frac{\partial\psi}{\partial t} = -\frac{\hbar^2}{2m_b}\nabla^2\psi + m_a(\Phi + V_t)\psi. \quad (2.8)$$

If using the NFW profile as the mass distribution of the host, then the tidal potential is given by

$$V_{t,NFW} = -2\pi G\rho_0 R_s^3 r^2 \{a\cos^2\theta + (2\cos^2\theta - \sin^2\theta)(b - c)\}, \quad (2.9)$$

where

$$a = \frac{1}{R(1 + \frac{R}{R_s})^2 R_s^2}, \quad (2.10)$$

$$b = \frac{1}{R^2(1 + \frac{R}{R_s})R_s}, \quad (2.11)$$

$$c = \frac{\ln(1 + \frac{R}{R_s})}{R^3}, \quad (2.12)$$

$\rho_0$  and the scale radius,  $R_s$ , are the parameters of NFW profile. By using the above function, we can simulate the three-dimensional evolution of soliton in the moving non-rotating frame and even use the more general tidal potential.





## Chapter 3 Numerical method

To investigate the evolution of perturbed soliton under the influence of tidal force, we use the code GAMER [23] and run the numerical simulation in the moving non-rotating frame. GAMER supports AMR and parallel GPU computing. Due to the heavy computation of simulating the Milky Way in the inertial frame, we simulate the tests in a moving non-rotating frame and focus on the circular orbit.

When we simulate in the moving non-rotating frame, a small box is sufficient to conduct it. However, in the scenario, there is a possibility that the object may touch the boundary and experience the rebound effect. This may affect the simulation. In order to prevent the dark matter from reaching the edges of the box boundary, we introduce a “sponge” into the outer regions of the grid. It will absorb the dark matter located too far away from the soliton. The absorption rate of the sponge is

$$damp(t) = e^{(-vt)}, \quad (3.1)$$

$$v(r) = 0.5a(1 + \tanh((r - b)/c)), \quad (3.2)$$

with the parameter  $\{a,b,c\} = \{2,20,5\}$  and  $t$  is the elapsed time. Density is multiplied by “damp” to reduce itself.



### 3.1 Construction of perturbed soliton

We use GAMER[23] to create a soliton without oscillations and introduce perturbations through the code from [5] to generate the desired oscillations. We apply the perturbation based on spherical symmetry to give disturbances.

Considering an unperturbed soliton with  $m_b = 8e-23$  eV in a no tidal field system, we manually introduce disturbances by adding spherically distributed FDM. Then, the soliton that has been perturbed will evolve until its oscillations stabilize and maintain spherical symmetry throughout its evolution. We determine the peak density ( $\rho_c$ ) of this oscillating soliton by calculating the time-averaged value of the peak density. In the top panel of Figure 3.1, it can be seen that the soliton, after being disturbed initially, quickly reached stable oscillation. Also, focusing on the black line which represents the density profile of the fitted soliton by the average peak density from the perturbed soliton, we can see the core is identifiable by the soliton profile as shown in the bottom panel of Figure 3.1.

### 3.2 Moving non-rotating frame system

Simulating the Milky Way in an inertial reference frame presents computational challenges. The main consideration is that in an inertial coordinate system. The orbital velocity needs to be provided as an input, while in the moving non-rotating coordinate system, it is not required. This difference means that an inertial coordinate system requires a higher resolution at the base level to ensure accuracy. Then it will cost more simulation time. Therefore, to shorten the simulation time, choosing the moving non-rotating coordinate system is a preferred option.

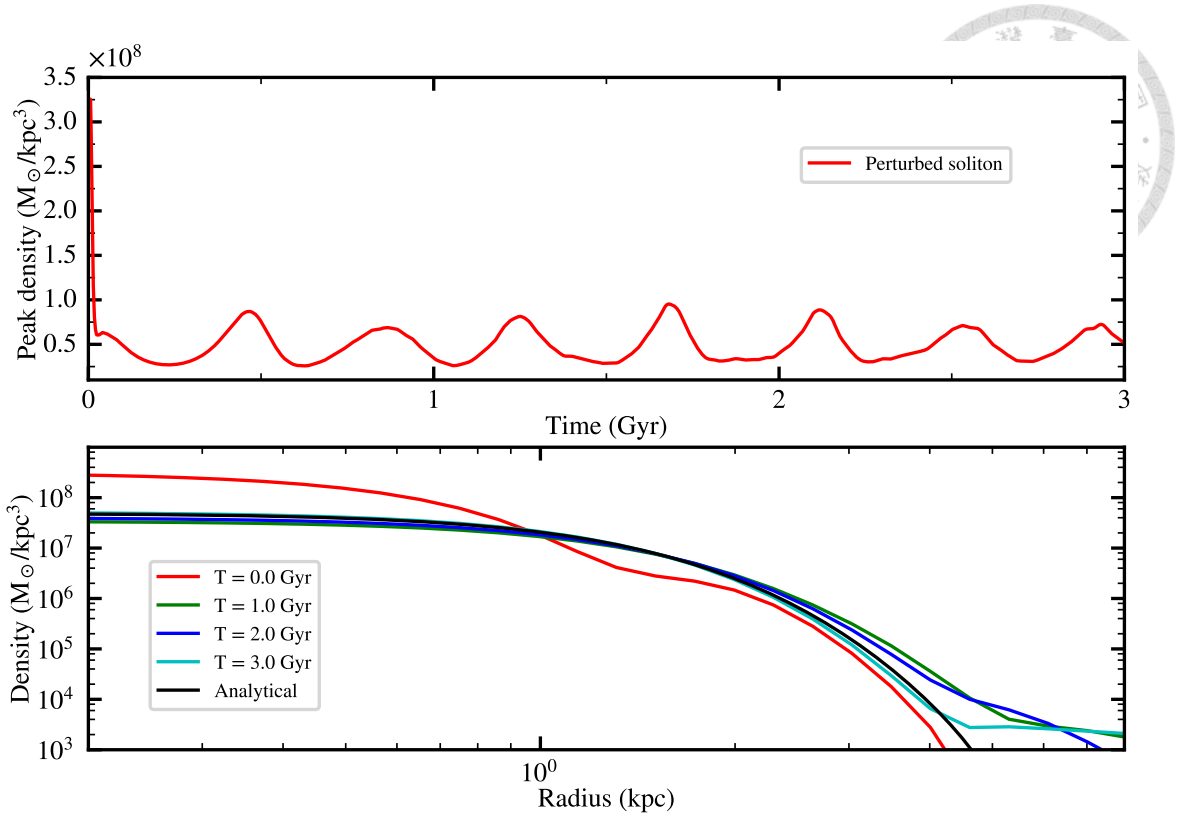
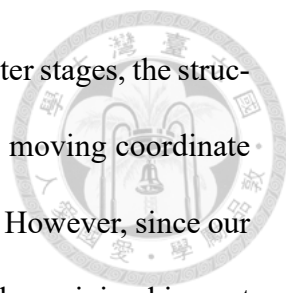


Figure 3.1: The evolution of perturbed soliton with  $\rho_c \approx 5.14e7 M_{\odot}kpc^{-3}$ . *Top*: Peak density of the perturbed soliton. The soliton reaches equilibrium in 0.5 Gyr. *Bottom*: Density profile of the perturbed soliton at different times. The black line represents the fitted profiles defined by Eq. (2.3) with an average  $\rho_c$ . It is evident that the cores are characterized by soliton profiles when it is stable.

In the moving non-rotating coordinate system, we can see the host orbits the coordinate origin that coincides with the center of mass of the soliton. The distinctive feature of this system compared to the typical rotating coordinate systems is that its coordinate axes do not rotate along with the center of mass of the soliton.

Based on our assumptions about deriving tidal potential, we are aware that placing solitons too close to the host will lead to problematic outcomes in the derivation. Here, we conducted a convergence test. We tested the scenario where a soliton is placed very close to the center in both the inertial coordinate system and the moving coordinate system to observe the differences between the two. We placed the soliton at a distance of 20 kpc from the host which is much smaller than other cases in our simulation. Figure 3.2 is the projection plot in both systems. we can see that the deformations in both cases are





remarkably similar in the early stage. As the evolution progresses to later stages, the structure becomes disrupted. Also, there are no higher-order forces in the moving coordinate system. We would observe the different deformation in both systems. However, since our goal is to observe the evolution of the soliton without disruption, this has minimal impact on our experimental focus.

In Figure 3.3, we delve deeper into the observation of the structural evolution of solitons. It compares the structural configuration of the soliton at various time points in both coordinate systems. Focusing on the bottom panel of relative errors, We can observe that the error within the interior of the soliton is minimal, whereas larger errors begin to appear outside the soliton. The larger error outside is due to the low-density values, where even a small difference can result in a significant error. However, since our experiment focuses on the high-density region of the soliton, this has minimal impact on our study. From Figure 3.3, we can conclude that despite placing the soliton very close to the host in this test, we still obtain convergent results. This provides us with assurance of accuracy for our experiment.

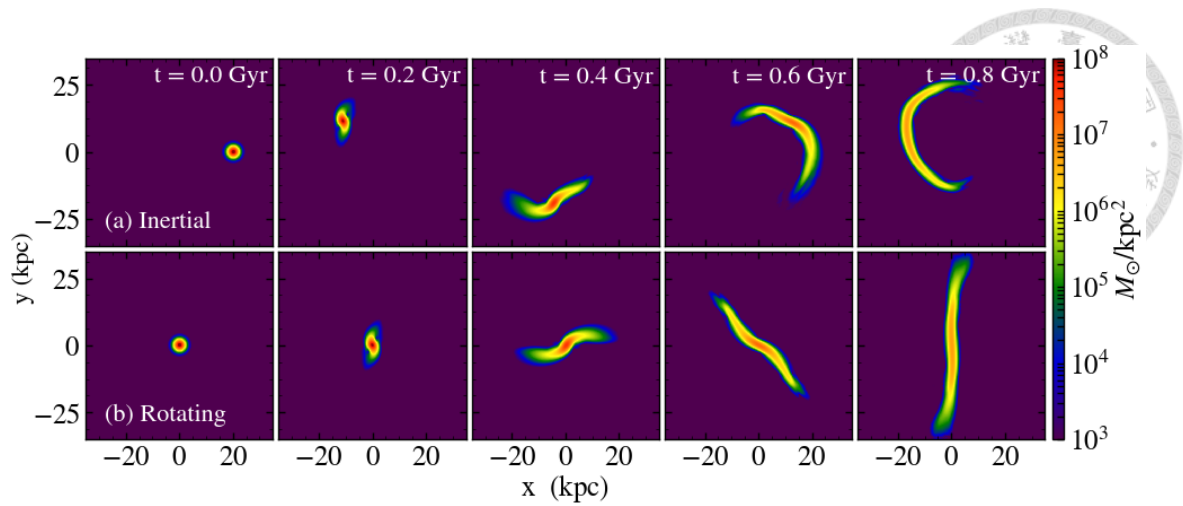


Figure 3.2: The projected soliton density at different times is shown for different coordinate systems. The top panel is the inertial coordinate and the bottom panel is the moving coordinate system. During the initial stages of evolution, the deformations are quite similar between the two. However, in the later stages, as the structure becomes disrupted, tidal forces elongate the soliton into a tail-like shape. Because there are no higher-order forces in the moving coordinate system, the shapes of the tails in the two systems differ.

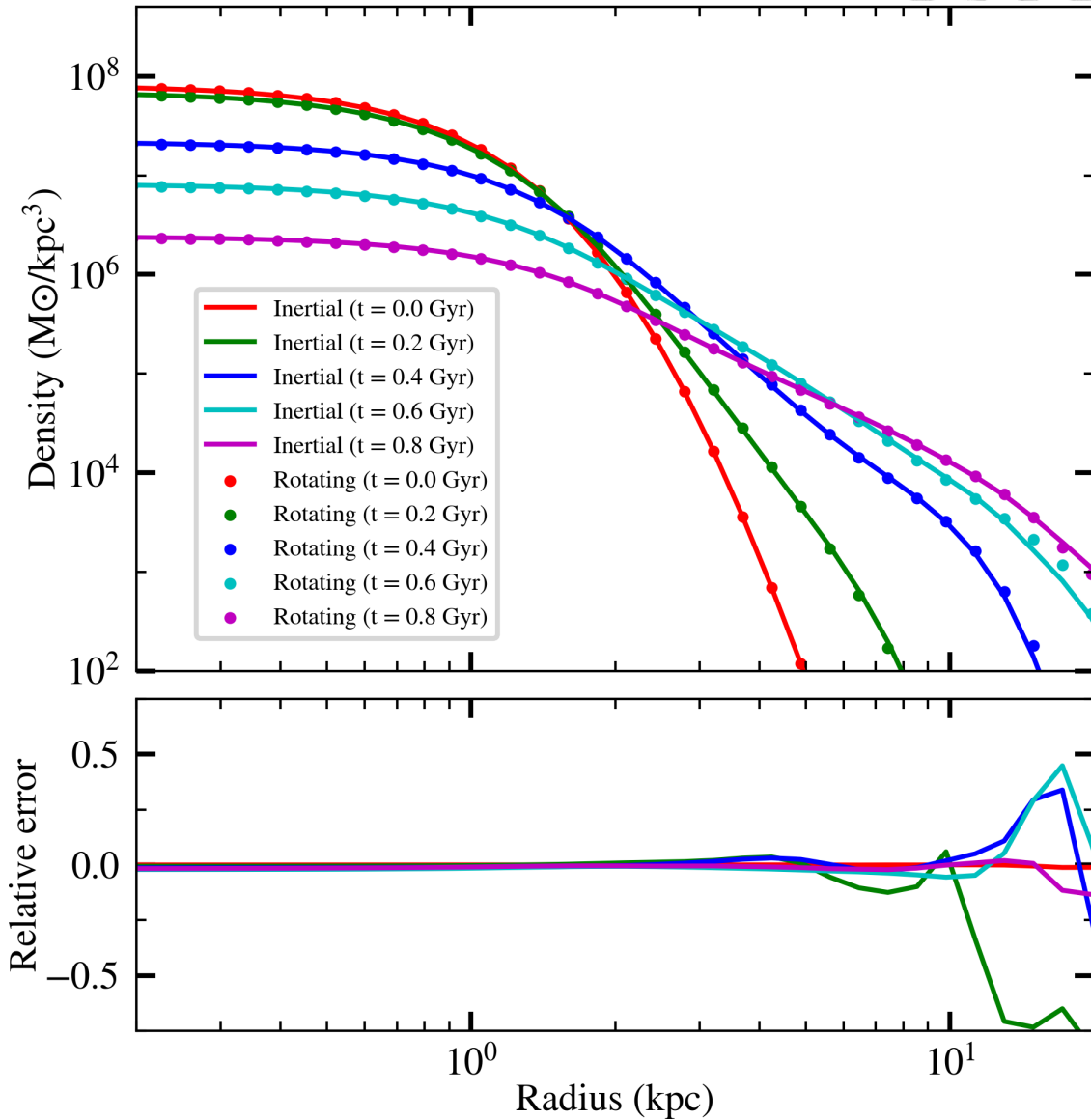


Figure 3.3: The structural evolution and relative error of soliton at different times. *Top:* Density profile of soliton at different times in different systems. In the inertial coordinate system, the representation is shown using lines, while in the moving coordinate system, it is depicted using dots. The data points within the higher-density internal region are largely consistent between the two systems. Differences in data points begin to emerge in the lower-density external region. *Bottom:* Relative error in both systems at different times. The error within the interior part of the soliton is minimal, while significant error is present in the exterior. From both panels, it is evident that the data in the high-density internal region of the two systems are in agreement. This region aligns with our experimental focus. However, there are slight discrepancies in the external region, primarily due to the lower density. As a result, the relative errors are larger in this region.



### 3.3 Simulation setup

We use the soliton in Figure 3.1 with an average  $r_c = 0.87$  kpc as the initial condition and perform numerical simulations to observe the evolution of perturbed soliton under the influence of tidal forces. In the simulation, we use adaptive mesh refinement to reduce the simulation time. AMR allows us to modify the resolution as desired. The grid spacing would be relatively wider in lower-density regions and finer in higher-density regions. The box has three sides of 50 kpc with a base grid of  $256^3$  and up to three refinement levels. Cells with  $\rho_{DM} > 10^{l+4}$  are refined to level  $l + 1$  for  $0 \leq l \leq 2$ , leading to a resolution of 0.024 kpc. We use 36 cells to resolve the core. This value is very enough to resolve the core of the soliton.

To easily describe the magnitude of tidal forces, we adopt the same approach in [7], using the initial density ratio  $\mu$  as the parameter.  $\mu$  is defined as

$$\mu = \frac{\rho_{soliton,peak}}{\bar{\rho}_{host}}, \quad (3.3)$$

where  $\bar{\rho}_{host}$  is the average density of the host within the radius of the orbit and  $\rho_{soliton,peak}$  is the average peak density of soliton. If the  $\mu$  is larger, the tidal force is weaker. We can vary the  $\mu$  by placing the soliton at different orbital radii.

To approximate the condition in Milky Way, we treat the host as a point mass with  $M_{host} = 1e12 M_{\odot}$ . Then, the tidal potential will follow Eq. (2.7). By placing soliton at different distances, We can test the evolution of soliton oscillations under different tidal forces. In these works, we run the simulation for 9 Gyr.





## Chapter 4 Simulation result

In this chapter, we present the result of the evolution of soliton with different initial density ratios  $\mu$  and calculate the decay of their oscillation amplitudes. We will categorize our results into three main regimes. The first regime is when the tidal forces are too strong and lead to the destruction of the soliton. The second regime is when the tidal force dampens the oscillation but does not destroy the soliton. The third regime is the soliton remains its structure and can sustain its oscillation.

### 4.1 Different regime

First, we show the result of three representative cases with  $\mu = 50, 120,$  and  $210$  introducing the three regimes of  $\mu$ . Figure 4.1 shows the projected soliton density, presenting the time evolution of soliton. When  $\mu$  is equal to  $210$  and  $120$ , it can survive for  $9$  Gyr. However, when  $\mu$  is equal to  $50$ , it is destroyed, meaning the central density decreases by more than one order of magnitude (as shown in the bottom panel in Figure 4.2). By further observing Figure 4.3, we can see the difference between  $\mu = 210$  and  $120$ . The oscillation amplitude still exists for  $\mu = 210$ , while it is almost disappearing for  $\mu = 120$ .

According to the results, we divide  $\mu$  into three different regimes. The three regimes can be distinguished based on the response of the system to tidal forces. In the first regime,

tidal forces have little effect on the oscillation amplitude. In the second regime, tidal forces affect the oscillation amplitude but do not alter the soliton structure (as shown in the middle panel of Figure 4.2). In the third regime, tidal forces not only affect the oscillation amplitude but also destroy the soliton structure.

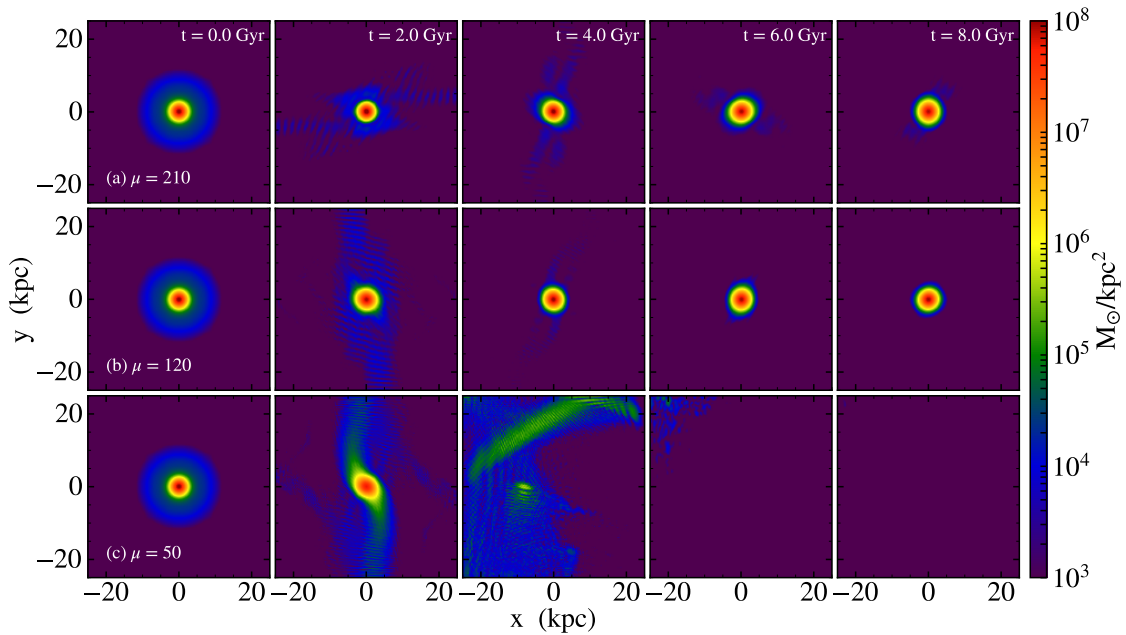
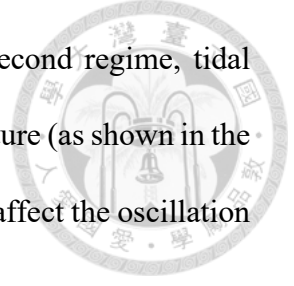


Figure 4.1: The projected soliton density at different times is shown for three initial density ratios:  $\mu = 50$ , 120, and 210. The top, middle, and bottom panels correspond to  $\mu = 210$ , 120, and 50. We show time slices taken at two-gigayear intervals. When tidal forces are weak, they do not have a significant effect on the soliton core, but when they are strong, they can destroy the soliton.

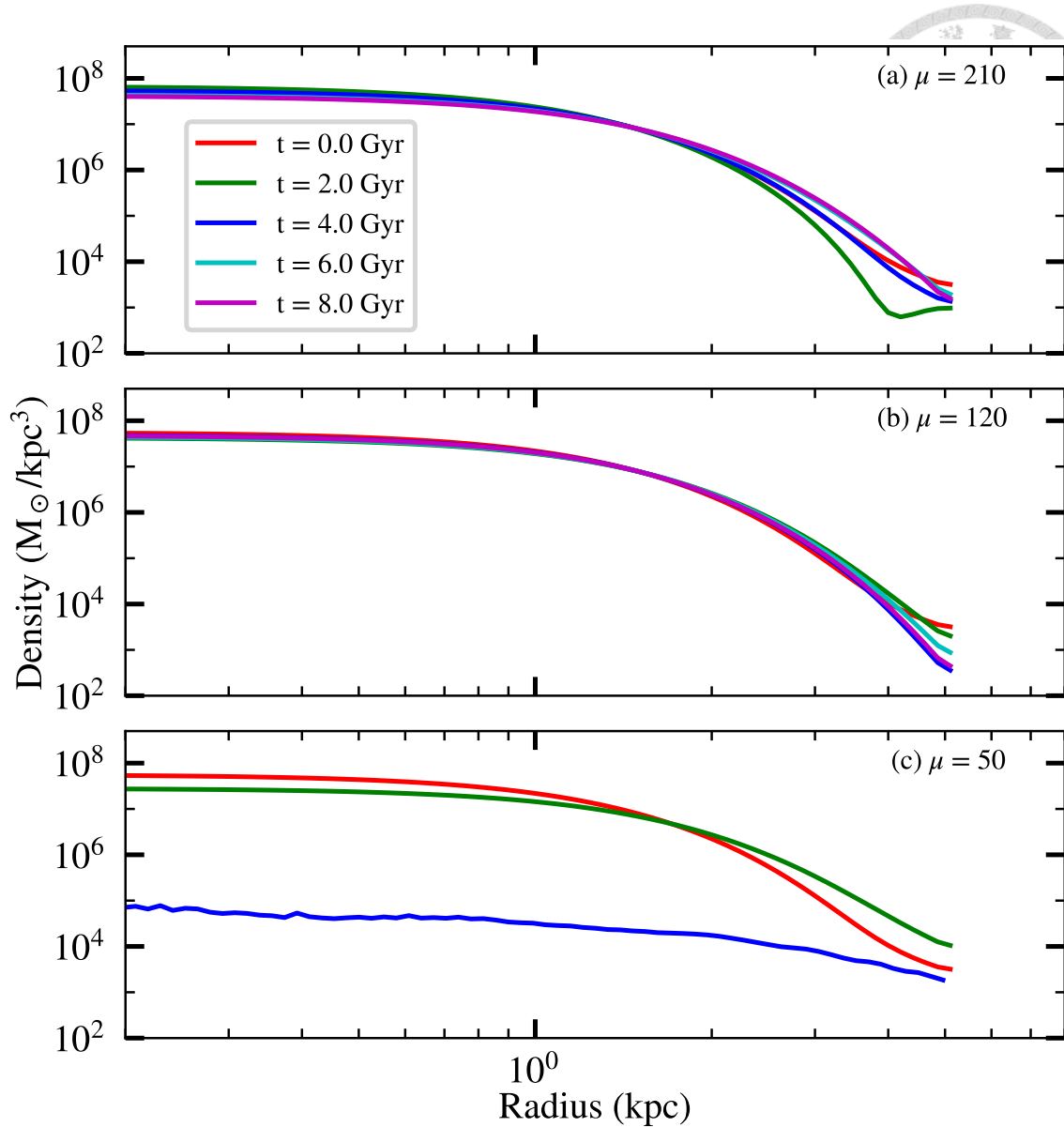


Figure 4.2: Density profile of soliton at different times for initial density ratios  $\mu = 50$ , 120, and 210. We plot the initial condition (red) and the configurations at  $t = 2.0$  (green), 4.0 (red), 6.0 (cyan), and 8.0 (purple) Gyr. We define the destruction of a soliton as a significant drop in central density by more than one order of magnitude. Therefore, when subjected to strong tidal forces, solitons cannot maintain their shape, and their central density drops by more than one order of magnitude, which we consider as being destroyed. However, when tidal forces are weak, solitons can maintain their shape without being destroyed.

## 4.2 Result comparison

We focus on the cases with  $\mu = 90$ , 120, 150, and 210 to illustrate our findings regarding the detailed variation of oscillation amplitude under tidal forces in the first and



second regimes. Figure 4.3 displays the temporal evolution of peak density oscillations, which reveals that the amplitude decreases and the oscillation period increases as time progresses. Moreover, as  $\mu$  becomes smaller, the rate at which the amplitude decreases increases. It can be observed that  $\mu = 210$  still exhibits a significant oscillation amplitude at 9 Gyr, whereas  $\mu = 90$  has almost no oscillations at 5 Gyr and remains stable at the subsequent time. Based on the above, we can confirm that tidal forces can reduce the oscillation of solitons. Under the strength that will not destroy solitons, the greater the tidal force, the faster the reduction rate.

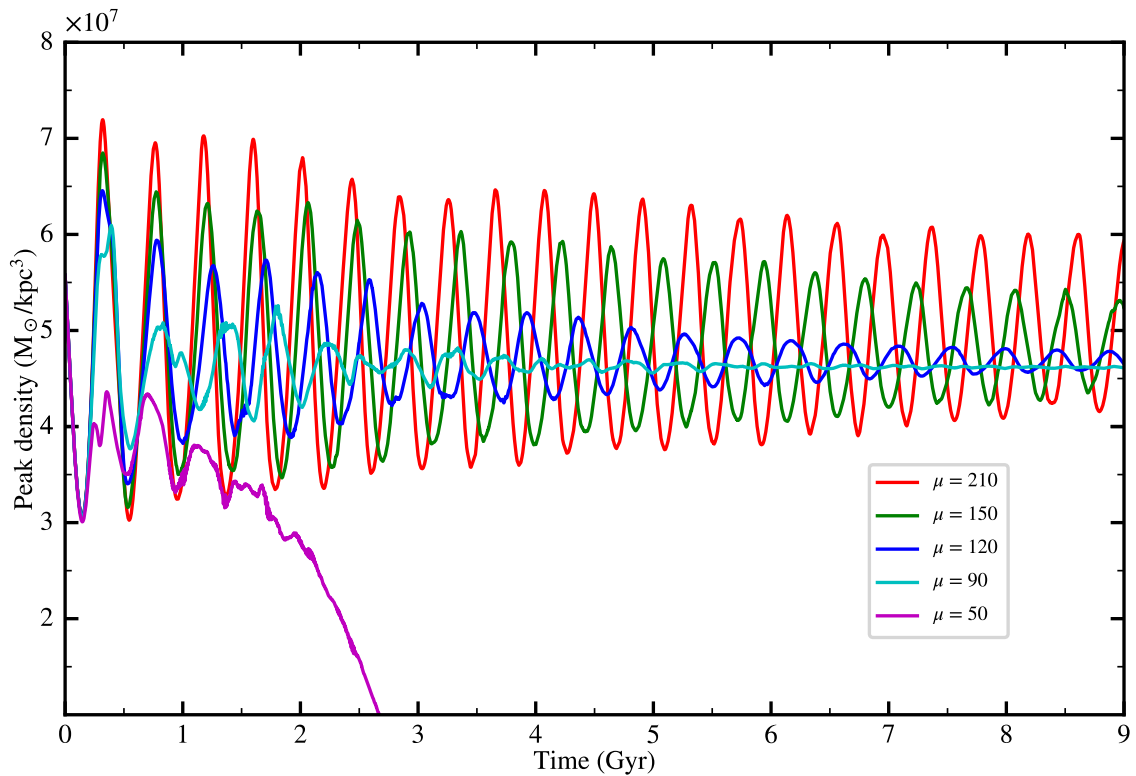
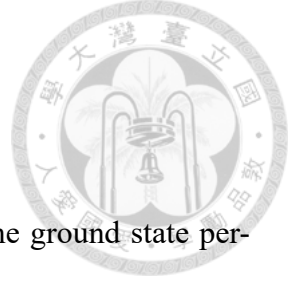


Figure 4.3: Time evolution of peak density for the initial density ratios  $\mu = 50$  (purple), 90 (cyan), 120 (blue), 150 (green), and 210 (red). All solitons in the tests evolved from the same initial peak density. It can be observed that as time progresses, the amplitude of soliton oscillation gradually decreases. Additionally, it is evident that as the tidal force increases, the rate at which the amplitude of soliton oscillation decreases increases as well.



### 4.3 Amplitude calculation

For further analysis of the results, we calculate the values of the ground state percentage and excited state percentage for each time. Assuming the wave function is only composed of the ground state and excited state. The definition of excited states in this context is based on considering all wave functions that are not in the ground state as excited states. Also, we assume the ground state and excited state are orthonormal.

$$\psi = a_1\psi_G + a_2\psi_E, \quad (4.1)$$

$$\langle\psi_G|\psi_E\rangle = 0, \quad (4.2)$$

where  $\psi_G$  is the ground state of the wave function, the  $\psi_E$  is the excited state, and the  $a_1$  and  $a_2$  is the coefficient. First, we normalize the wave function,

$$\psi_{normalize} = \frac{a_1}{\sqrt{a_1^2 + a_2^2}}\psi_G + \frac{a_2}{\sqrt{a_1^2 + a_2^2}}\psi_E, \quad (4.3)$$

and determine the density profile of the ground state ( $\psi_G$ ) by taking the average peak density over the last gigayear in the simulation and reforming the perfect soliton that represents the ground state from the Eq (2.3). Due to the orthogonal of the ground state and the excited state, we do the inner product of the normalized simulated density profile and the normalized density profile of the ground state,

$$\langle\psi_{g,normalize}|\psi_{normalize}\rangle = \frac{a_1}{\sqrt{a_1^2 + a_2^2}}, \quad (4.4)$$

we define the squared value of the resulting quantity as the ground state percentage, and the excited state percentage is defined as 1 minus the ground state percentage. Ensuring that

the sum of the numerical values of the two percentages equals one. With such a definition, we can plot the state percentage as a function of time to depict its evolution over time and be more illuminating,

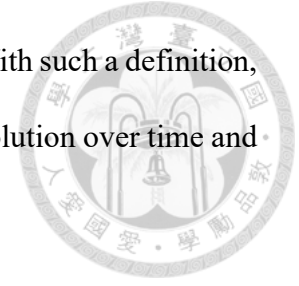
$$\text{Ground state percentage} \equiv \frac{a_1^2}{a_1^2 + a_2^2}, \quad (4.5)$$

$$\text{Excited state percentage} \equiv 1 - \frac{a_1^2}{a_1^2 + a_2^2}. \quad (4.6)$$

Also, we introduce the window function to do the window average using a filter size of ten. It can help us observe more pronounced features. Due to inconsistent ground state selection, even for the same soliton, there may be variations in the calculated initial values on the graph. However, this does not affect our ability to observe the trend of evolution.

From [5], We believe the oscillation amplitude would be influenced by the ratio of  $a_1$  and  $a_2$ . If the ratio of  $a_1$  to  $a_2$  is larger, the amplitude will be also larger. According to the observation that the amplitude continuously decreases in Figure 4.2, we conjecture that the ratio of  $a_1$  and  $a_2$ . will also decrease over time. Figure 4.4 provides additional confirmation, illustrating the temporal evolution of the ground state percentage in the upper panel and the excited state percentage in the lower panel. As time evolves, the ground state percentage increases and the excited state percentage decreases. Consequently, the ratio of the ground state percentage to the excited state percentage decreases over time.

In addition, we also observe that with the increase of tidal forces, the aforementioned process also accelerates. Based on consistent results with previous findings of the oscillation amplitude, we believe that tidal forces can diminish the excited state of solitons, thereby reducing their oscillation. For a given soliton, the stronger the tidal forces, the stronger this effect becomes. However, when tidal forces exceed a certain threshold, they



can directly destroy the soliton.

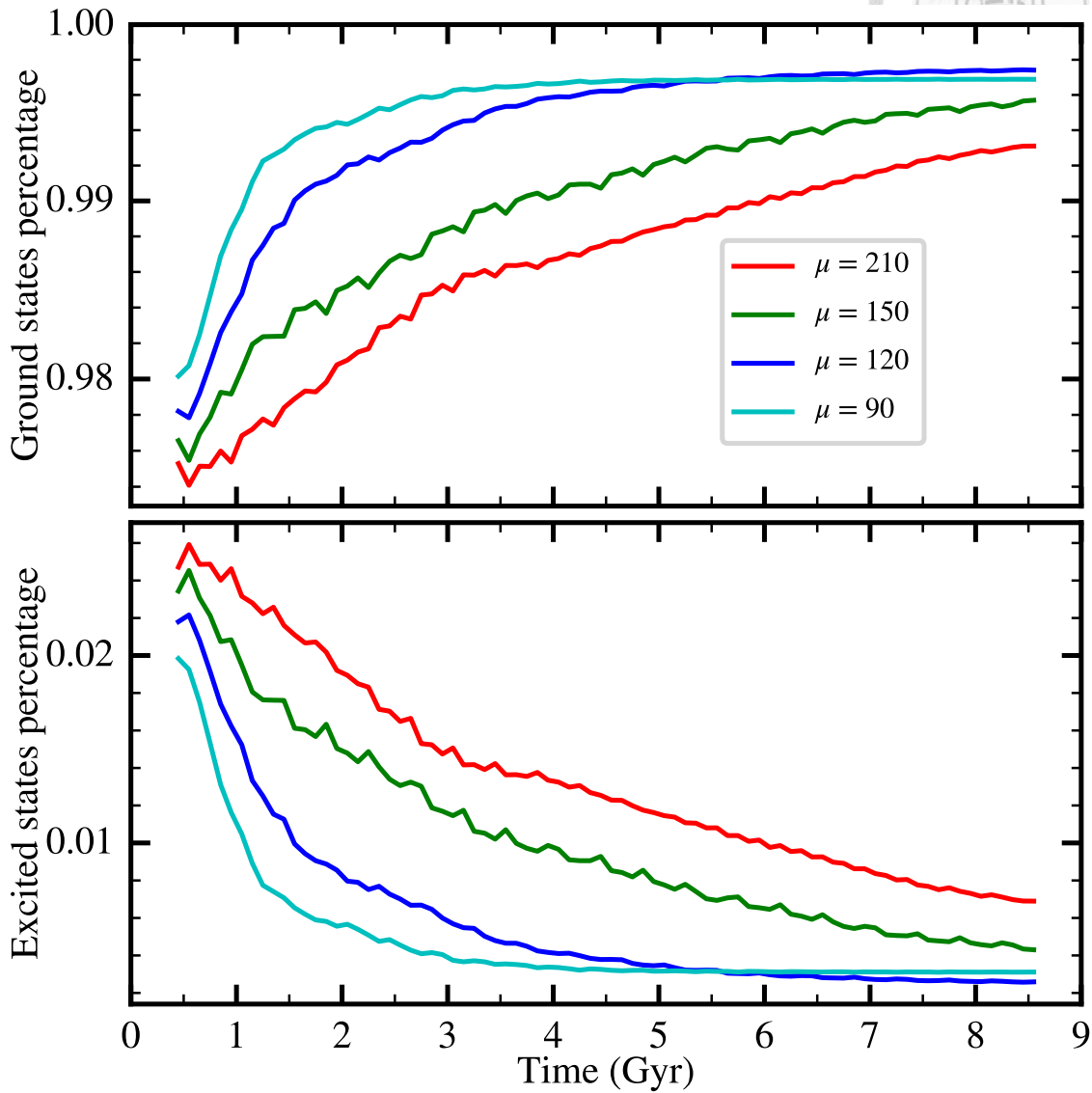
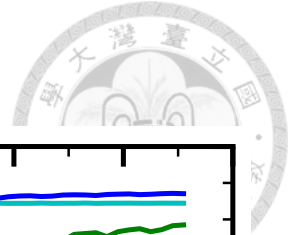
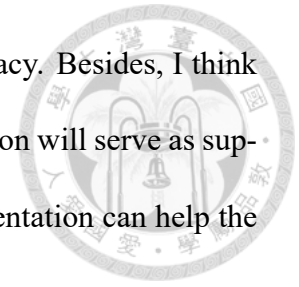


Figure 4.4: *Top*: Time evolution of ground state percentage for the initial density ratios  $\mu = 50$  (purple), 90 (cyan), 120 (blue), 150 (green), and 210 (red). *Bottom*: Time evolution of excited state percentage. As time progresses, the ground state percentage increases while the excited state percentage decreases. When the tidal forces increase, this process speeds up. It demonstrates that tidal forces, depending on their strength, remove the excited state over time

## 4.4 Future work

About future work, I think the most important thing is how to quantify the decay rate of oscillation. Completing the quantification of the decay rate allows for comparison

with other works or observational data, thereby enhancing the accuracy. Besides, I think testing the different host mass distributions and amplitude of oscillation will serve as supplementary evidence of generality. Last, The elliptical orbit implementation can help the simulation be more realistic.





## Chapter 5 Conclusion

In order to understand the evolution of soliton under the influence of tidal disruption, we performed various numerical simulations and analyses on soliton. Making the assumption that the radius of the soliton is significantly smaller than the distance from the soliton to the host, allows us to derive the tidal potential in the rotating coordinate system. Also, we only consider purely circular orbits, enabling us to perform simulations in a rotating coordinate system. These approaches help us gain a more intuitive understanding of the physical meaning behind the phenomena we are studying.

We vary the orbital radius to control the magnitude of tidal forces. The evolution of the oscillating soliton will vary under different tidal forces as well. During our simulations, we observe that larger tidal forces result in faster damping of the soliton oscillations. When the tidal forces become stronger than a certain threshold, they can ultimately lead to the destruction of the soliton.

After further analysis of this phenomenon, we present a plot showcasing the evolution of the percentage of the ground state and the excited state of the soliton over time. We reconfirm the aforementioned conclusion and observe that tidal force removes the excited states of the soliton, resulting in the damping of its oscillations. Additionally, we noted that larger tidal forces lead to faster removal of the excited states. These findings align

with our expectations.

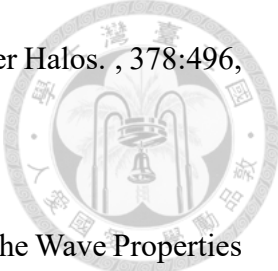


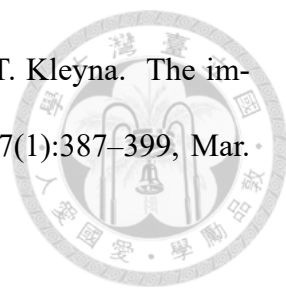


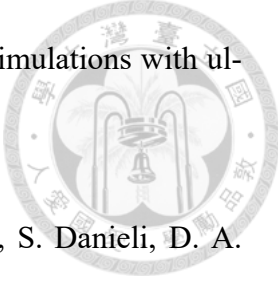
## References

- [1] E. Armengaud, N. Palanque-Delabrouille, C. Yèche, D. J. E. Marsh, and J. Baur. Constraining the mass of light bosonic dark matter using SDSS Lyman- $\alpha$  forest. , 471(4):4606–4614, Nov. 2017.
- [2] M. Boylan-Kolchin, J. S. Bullock, and M. Kaplinghat. Too big to fail? The puzzling darkness of massive Milky Way subhaloes. , 415(1):L40–L44, July 2011.
- [3] S.-R. Chen, H.-Y. Schive, and T. Chiueh. Jeans analysis for dwarf spheroidal galaxies in wave dark matter. , 468(2):1338–1348, June 2017.
- [4] B. T. Chiang, H.-Y. Schive, and T. Chiueh. Soliton oscillations and revised constraints from Eridanus II of fuzzy dark matter. , 103(10):103019, May 2021.
- [5] T. Chiueh and Y.-H. Hsu. Theory and phenomenology of stressed wave-dark-matter soliton. , 107(6):063011, Mar. 2023.
- [6] X. Du, C. Behrens, and J. C. Niemeyer. Substructure of fuzzy dark matter haloes. , 465(1):941–951, Feb. 2017.
- [7] X. Du, B. Schwabe, J. C. Niemeyer, and D. Bürger. Tidal disruption of fuzzy dark matter subhalo cores. , 97(6):063507, Mar. 2018.



- 
- [8] J. Dubinski and R. G. Carlberg. The Structure of Cold Dark Matter Halos. , 378:496, Sept. 1991.
- [9] W. Hu, R. Barkana, and A. Gruzinov. Fuzzy Cold Dark Matter: The Wave Properties of Ultralight Particles. , 85(6):1158–1161, Aug. 2000.
- [10] L. Hui, J. P. Ostriker, S. Tremaine, and E. Witten. Ultralight scalars as cosmological dark matter. , 95(4):043541, Feb. 2017.
- [11] S. U. Ji and S. J. Sin. Late-time phase transition and the galactic halo as a Bose liquid. II. The effect of visible matter. , 50(6):3655–3659, Sept. 1994.
- [12] A. Klypin, A. V. Kravtsov, O. Valenzuela, and F. Prada. Where Are the Missing Galactic Satellites? , 522(1):82–92, Sept. 1999.
- [13] T. Kobayashi, R. Murgia, A. De Simone, V. Iršič, and M. Viel. Lyman- $\alpha$  constraints on ultralight scalar dark matter: Implications for the early and late universe. , 96(12):123514, Dec. 2017.
- [14] D. J. E. Marsh and J. C. Niemeyer. Strong Constraints on Fuzzy Dark Matter from Ultrafaint Dwarf Galaxy Eridanus II. , 123(5):051103, Aug. 2019.
- [15] B. Moore. Evidence against dissipation-less dark matter from observations of galaxy haloes. , 370(6491):629–631, Aug. 1994.
- [16] B. Moore, S. Ghigna, F. Governato, G. Lake, T. Quinn, J. Stadel, and P. Tozzi. Dark Matter Substructure within Galactic Halos. , 524(1):L19–L22, Oct. 1999.
- [17] J. F. Navarro, C. S. Frenk, and S. D. M. White. A Universal Density Profile from Hierarchical Clustering. , 490(2):493–508, Dec. 1997.

- 
- [18] J. I. Read, M. I. Wilkinson, N. W. Evans, G. Gilmore, and J. T. Kleya. The importance of tides for the Local Group dwarf spheroidals. , 367(1):387–399, Mar. 2006.
- [19] V. Sahni and L. Wang. New cosmological model of quintessence and dark matter. , 62(10):103517, Nov. 2000.
- [20] H.-Y. Schive, T. Chiueh, and T. Broadhurst. Cosmic structure as the quantum interference of a coherent dark wave. Nature Physics, 10(7):496–499, July 2014.
- [21] H.-Y. Schive, T. Chiueh, and T. Broadhurst. Soliton Random Walk and the Cluster-Stripping Problem in Ultralight Dark Matter. , 124(20):201301, May 2020.
- [22] H.-Y. Schive, M.-H. Liao, T.-P. Woo, S.-K. Wong, T. Chiueh, T. Broadhurst, and W. Y. P. Hwang. Understanding the Core-Halo Relation of Quantum Wave Dark Matter from 3D Simulations. , 113(26):261302, Dec. 2014.
- [23] H.-Y. Schive, J. A. ZuHone, N. J. Goldbaum, M. J. Turk, M. Gaspari, and C.-Y. Cheng. GAMER-2: a GPU-accelerated adaptive mesh refinement code - accuracy, performance, and scalability. , 481(4):4815–4840, Dec. 2018.
- [24] B. Schwabe, J. C. Niemeyer, and J. F. Engels. Simulations of solitonic core mergers in ultralight axion dark matter cosmologies. , 94(4):043513, Aug. 2016.
- [25] E. Seidel and W.-M. Suen. Dynamical evolution of boson stars: Perturbing the ground state. , 42(2):384–403, July 1990.
- [26] P. Svrcek and E. Witten. Axions in string theory. Journal of High Energy Physics, 2006(6):051, June 2006.

- 
- [27] J. Veltmaat and J. C. Niemeyer. Cosmological particle-in-cell simulations with ultralight axion dark matter. , 94(12):123523, Dec. 2016.
- [28] A. Wasserman, P. van Dokkum, A. J. Romanowsky, J. Brodie, S. Danieli, D. A. Forbes, R. Abraham, C. Martin, M. Matuszewski, A. Villaume, J. Tamanas, and S. Profumo. Spatially Resolved Stellar Kinematics of the Ultra-diffuse Galaxy Dragonfly 44. II. Constraints on Fuzzy Dark Matter. , 885(2):155, Nov. 2019.
- [29] L. M. Widrow and N. Kaiser. Using the Schroedinger Equation to Simulate Collisionless Matter. , 416:L71, Oct. 1993.



# Appendix A — tidal potential derivation and $\mu$ in different frames

We presented tidal potential in Chapter 2 and utilized it as an external field in the simulation. We will now demonstrate how we derived this formula. First, let's consider a satellite orbiting a point mass,  $M$ , and assume that the satellite radius,  $r$ , is significantly smaller than the distance between the center of mass of the satellite and the host,  $R$ . The satellite experiences the gravitational influence of the point mass.

$$F(R) = -\frac{GM}{R^2}, \quad (\text{A.1})$$

We choose a point on the surface of the satellite and its distance to the host is denoted as  $D$ . Due to the variation in the gravitational field, the satellite is subjected to tidal forces.

$$F_T = F(\vec{D}) - F(\vec{R}) = F(\vec{R} + \vec{r}) - F(\vec{R}) = r\nabla F(\vec{R}), \quad (\text{A.2})$$

The following is the subsequent derivation.



$$\begin{aligned}
F_T &= r \frac{\partial}{\partial r} \frac{-GM}{R^2} \hat{R}, \\
&= r \left( \frac{\partial}{\partial r} \frac{-GM}{R^3} \right) \vec{R} + r \frac{-GM}{R^3} \frac{\partial}{\partial r} \vec{R}, \\
&= r \left( \frac{\partial}{\partial R} \frac{\partial R}{\partial r} \frac{-GM}{R^3} \right) \vec{R} + \frac{-GM}{R^3} \vec{r}, \\
&= r \cos \theta \frac{GM}{R^4} \vec{R} + \frac{-GM}{R^3} \vec{r}, \\
&= r \cos \theta \frac{GM}{R^3} \hat{R} + r \frac{-GM}{R^3} \hat{r}, \\
&= \frac{GM r}{R^3} (2 \cos^2 \theta - \sin^2 \theta) \hat{r} + \frac{-3GM r}{R^3} \cos \theta \sin \theta \hat{\theta}, \tag{A.3}
\end{aligned}$$

where

$$\hat{R} = \frac{\vec{R}}{R} = \cos \theta \hat{r} - \sin \theta \hat{\theta}, \tag{A.4}$$

$$\frac{\partial}{\partial r} = \frac{\partial}{\partial R} \frac{\partial R}{\partial r} = \cos \theta \frac{\partial}{\partial R}, \tag{A.5}$$

$$r \frac{\partial}{\partial r} \vec{R} \approx (\vec{R} + \vec{r}) - \vec{R} = \vec{r}. \tag{A.6}$$

After completing the calculations mentioned above, we can obtain the results for Chapter 2. Next, we proceed to calculate the central halo assuming the NFW profile as the mass distribution. We will use the same calculation method as for the point mass, but the central density distribution and mass will be modified to fit the NFW profile.

$$\rho(R) = \frac{\rho_0}{\frac{R}{R_s} \left(1 + \frac{R}{R_s}\right)^2} \tag{A.7}$$

$$F(R) = -4\pi G \rho_0 R_s^3 \left( \frac{-1}{R \left(1 + \frac{R}{R_s}\right) R_s} + \frac{\ln \left(1 + \frac{R}{R_s}\right)}{R^2} \right) \tag{A.8}$$

Now, let us continue with the subsequent derivation.



$$\begin{aligned}
 F_T &= r \nabla F(\vec{R}) \\
 &= -4\pi G \rho_0 R_s^3 \left[ r \frac{\partial}{\partial r} \left( \frac{-1}{R(1 + \frac{R}{R_s})R_s} + \frac{\ln(1 + \frac{R}{R_s})}{R^2} \right) \hat{R} \right] \\
 &= -4\pi G \rho_0 R_s^3 \left[ r \frac{\partial}{\partial r} \left( \frac{-1}{R^2(1 + \frac{R}{R_s})R_s} + \frac{\ln(1 + \frac{R}{R_s})}{R^3} \right) \vec{R} \right. \\
 &\quad \left. + r \left( \frac{-1}{R^2(1 + \frac{R}{R_s})R_s} + \frac{\ln(1 + \frac{R}{R_s})}{R^3} \right) \frac{\partial}{\partial r} \vec{R} \right] \\
 &= -4\pi G \rho_0 R_s^3 \left[ r \cos \theta \left( \frac{1}{R^2(1 + \frac{R}{R_s})R_s^2} + \frac{3}{R^3(1 + \frac{R}{R_s})R_s} + \frac{-3 \ln(1 + \frac{R}{R_s})}{R^4} \right) \vec{R} \right. \\
 &\quad \left. + \left( \frac{-1}{R^2(1 + \frac{R}{R_s})R_s} + \frac{\ln(1 + \frac{R}{R_s})}{R^3} \right) \vec{r} \right] \\
 &= -4\pi G \rho_0 R_s^3 r \left[ \left( \cos^2 \theta \frac{1}{R(1 + \frac{R}{R_s})R_s^2} \right. \right. \\
 &\quad \left. \left. + (2 \cos^2 \theta - \sin^2 \theta) \left( \frac{1}{R^2(1 + \frac{R}{R_s})R_s} - \frac{\ln(1 + \frac{R}{R_s})}{R^3} \right) \hat{r} \right) \right. \\
 &\quad \left. - \left( \cos \theta \sin \theta \frac{1}{R(1 + \frac{R}{R_s})R_s^2} \right. \right. \\
 &\quad \left. \left. - 3 \cos \theta \sin \theta \left( \frac{1}{R^2(1 + \frac{R}{R_s})R_s} - \frac{\ln(1 + \frac{R}{R_s})}{R^3} \right) \hat{\theta} \right) \right] \tag{A.9}
 \end{aligned}$$

Finally, we get the result of the NFW profile. With these results, we can simulate the test in a rotating coordinate system.





## Appendix B — calculate the amplitude

In this appendix, we will explain how to calculate the amplitude percentage using the simulation results by the method in Chapter 4.

The main purpose is to calculate the following formula,

$$|\langle \psi_{G,normalize} | \psi_{normalize} \rangle|^2 = \left| \int 4\pi r^2 \psi_{G,normalize}^* \psi_{normalize} dr \right|^2 = \frac{a_1^2}{a_1^2 + a_2^2}, \quad (\text{B.10})$$

the wave function of soliton is stored in the form of real and imaginary parts in the simulated data, which can be present as

$$\psi(r) = R(r) + I(r), \quad (\text{B.11})$$

We calculate the average density of the soliton over the last 1 Gyr in the simulation and use it to create soliton data with only the ground state by GAMER. Since we are using the first output data, the wave function of the soliton data with only the ground state will only have the real part, which can be present as

$$\psi_G(r) = R_G(r), \quad (\text{B.12})$$

Next, we normalize their wave function by dividing each of them by the square root of their respective soliton mass. Afterward, we take the normalized wave functions and use them



to perform the calculation according to equation B.10. After obtaining the calculation result, we apply a window function. It will average the data points using a window size of ten. By applying a window function, we can remove local variations that are not of interest to us and focus on the global trends we want to observe.

